

Document downloaded from:

<http://hdl.handle.net/10251/140989>

This paper must be cited as:

Zhang, D.; Valverde-Muñoz, FJ.; Bartual-Murgui, C.; Piñeiro-López, L.; Muñoz Roca, MDC.; Real, JA. (2018). $\{[\text{Hg}(\text{SCN})_3]_2(\text{n-L})\}_2$ -: An Efficient Secondary Building Unit for the Synthesis of 2D Iron(II) Spin-Crossover Coordination Polymers. *Inorganic Chemistry*. 57(3):1562-1571. <https://doi.org/10.1021/acs.inorgchem.7b02906>



The final publication is available at

<https://doi.org/10.1021/acs.inorgchem.7b02906>

Copyright American Chemical Society

Additional Information

{[Hg(SCN)₃]₂(μ-L)}²⁻: An Efficient Secondary Building Unit for the Synthesis of 2D Iron(II) Spin-Crossover Coordination Polymers

Daopeng Zhang,^{†,‡} Francisco Javier Valverde-Muñoz,[†] Carlos Bartual-Murgui,[†] Lucía Piñeiro-López,[†] M. Carmen Muñoz,[§] and José Antonio Real^{*,†} 

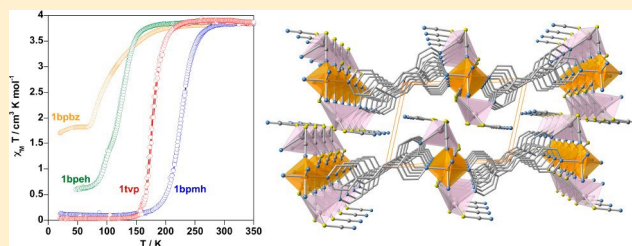
[†]Instituto de Ciencia Molecular (ICMol), Universitat de València, C/Catedrático José Beltrán Martínez 2, 46980 Paterna (Valencia), Spain

[‡]College of Chemical Engineering, Shandong University of Technology, Zibo 255049, People's Republic of China

[§]Departamento de Física Aplicada, Universitat Politècnica de València, Camino de Vera s/n, E-46022 Valencia, Spain

^{*}Supporting Information

ABSTRACT: We report an unprecedented series of two-dimensional (2D) spin-crossover (SCO) heterobimetallic coordination polymers generically formulated as {Fe^{II}[(Hg^{II}(SCN)₃]₂(L)_x}·Solv, where $x = 2$ for L = tvp (*trans*-(4,4'-vinylenedipyridine)) (1tvp), bpmh ((1*E*,2*E*)-1,2-bis(pyridin-4-ylmethylene)hydrazine) (1bpmh·*n*CH₃OH; $n = 0, 1$), bpeh ((1*E*,2*E*)-1,2-bis(1-(pyridin-4-yl)ethylidene)hydrazine) (1bpeh·*n*H₂O; $n = 0, 1$) and $x = 2.33$ for L = bpbz (1,4-bis(pyridin-4-yl)benzene) (1bpbz·*n*H₂O; $n = 0, 2/3$). The results confirm that self-assembly of Fe^{II}, [Hg^{II}(SCN)₄]²⁻, and ditopic rodlike bridging ligands L containing 4-pyridyl moieties favors the formation of linear [Fe(μ-L)]_{*n*}^{2*n+*} chains and in situ generated binuclear units {[Hg^{II}(SCN)₃]₂(μ-L)}²⁻. The latter act as bridges between adjacent chains generating robust 2D layers. The [Fe^{II}N₆] centers are equatorially surrounded by four NCS⁻ groups and two axial N atoms of the organic ligand L. The compound 1tvp and the unsolvated form of 1bpmh undergo complete SCO centered at $T_{1/2} = 177$ and 226 K, characterized by the enthalpy and entropy variations $\Delta H = 12.3$ and 10.5 kJ mol⁻¹ and $\Delta S = 69.4$ and 48 J K⁻¹ mol⁻¹, respectively. The almost complete SCO of the unsolvated form of 1bpeh occurs at ca. $T_{1/2} = 119$ K and exhibits a complete LIESST effect. Regardless of the degree of solvation, a half-spin conversion at $T_{1/2} < 100$ K occurs for 1bpbz·*n*H₂O, which becomes almost complete at $p = 0.65$ GPa. The labile solvent molecules present in 1bpmh·CH₃OH and 1bpeh·H₂O have a dramatic influence on the corresponding SCO behavior.



INTRODUCTION

Fe^{II} spin-crossover (SCO) compounds are excellent examples of heat-, pressure-, and light-induced phase transitions triggered by strong electron-phonon coupling. This coupling occurs when the difference between the energy gap defined by the e_g - t_{2g} orbitals in octahedral symmetry ($10Dq$) and the average interelectronic repulsion energy is close to $k_B T$. In the case of Fe^{II}, it involves a reversible transfer of two electrons between the e_g and t_{2g} orbitals and concomitant switch of the electronic structure between the high-spin (HS; $S = 2$) and the low-spin (LS; $S = 0$) states. This reversible transfer of electrons is accompanied by significant changes in bond lengths and angles of the Fe^{II} coordination sphere, which modify the shape and size of the complex, thereby influencing the elastic interactions (contacts between the active SCO centers), which are at the origin of the structural changes observed in the crystal. The elastic interactions determine the cooperativeness (gradual or abrupt) and the shape (i.e., steps) of the SCO.¹ In particular, strong elastic interactions confer bistability to the magnetic, optical, and electrical properties, making the resulting cooperative SCO compounds some of the most application-oriented examples of bistability in molecular materials.²

Cooperativity occurs when the spin state change of the individual SCO centers is synchronized through efficient hydrogen bonding, π - π intermolecular interactions, and/or rigid coordination bonds. The first two interactions prevail in discrete Fe^{II} SCO compounds (mononuclear or polynuclear), while the last predominates in one-, two-, and three-dimensional (1–3D) Fe^{II} SCO coordination polymers (SCO-CPs).³ Currently, one of the most investigated approaches to systematically synthesize Fe^{II} SCO-CPs involves the use of metalocyanate bridging ligands [M^I(CN)₂]⁻ (M^I = Cu, Ag, Au) and [M^{II}(CN)₄]²⁻ (M^{II} = Ni, Pd, Pt) in combination with monodentate or bisonodentate pyridyl-like ligands. This approach has afforded a rich variety of 2D and 3D polymeric structures and porous metal-organic frameworks with interesting host-guest dependent SCO properties.⁴ Extension of this idea to hexa- and octacyanometalate building blocks has so far afforded only two, but very interesting, Fe^{II} SCO-CPs based on the [Cr(CN)₆]³⁻ and [Nb(CN)₈]⁴⁻ units.⁵

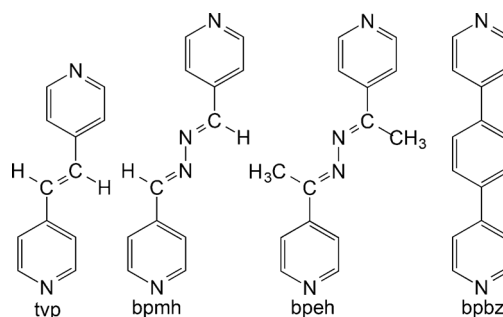
Searching for new metalloligand building blocks, we proposed the tetrathiocyanopalladate anion $[\text{Pd}(\text{SCN})_4]^{2-}$ as a suitable bridging unit for the generation of new Fe^{II} SCO-CPs.⁶ Indeed, self-assembly of Fe^{II} , pyrazine, and $[\text{Pd}(\text{SCN})_4]^{2-}$ afforded the compound $\{\text{Fe}(\text{pyrazine})[\text{Pd}(\text{SCN})_4]\}$, a 3D porous metal-organic framework structurally related to the SCO Hofmann-like system $\{\text{Fe}(\text{pyrazine})[\text{M}(\text{CN})_4]\}$ ($\text{M} = \text{Ni}, \text{Pd}, \text{Pt}$). In contrast to the latter compounds, $\{\text{Fe}(\text{pyrazine})[\text{Pd}(\text{SCN})_4]\}$ is HS at all temperatures at ambient pressure and only displays a gradual SCO behavior at high pressures (0.5–1.0 GPa). This fact prompted us to investigate alternative strategies. In this respect, we recently focused our attention on the possibilities of $[\text{Hg}(\text{SCN})_4]^{2-}$ tetrahedral species as efficient building blocks in the synthesis of new iron(II) SCO-CPs. Thus, self-assembly of Fe^{II} , 4,4'-bipyridine (4,4'-bipy), and $[\text{Hg}(\text{SCN})_4]^{2-}$ afforded in good yield a highly crystalline material formulated as $\{\text{Fe}^{\text{II}}[\text{Hg}^{\text{II}}(\text{SCN})_4]_2(\mu\text{-}4,4'\text{-bipy})_2\}^{2-}$ (1bipy), whose structure consists of linear $[\text{Fe}(\mu\text{-}4,4'\text{-bipy})]^{2+}$ chains linked by in situ generated $\{[\text{Hg}^{\text{II}}(\text{SCN})_4]^{2-}(\mu\text{-}4,4'\text{-bipy})\}_2$ anionic dimers, thereby defining an infinite stack of 2D CPs. This compound displays a three-step SCO behavior with symmetry-breaking transitions separating different ordered $[n\text{HS}:m\text{LS}]$ crystallographically characterized spin states: namely, $[0\text{HS}:1\text{LS}] \leftrightarrow \sim[1\text{HS}:2\text{LS}] \leftrightarrow [1\text{HS}:1\text{LS}] \leftrightarrow [1\text{HS}:0\text{LS}]$.⁸ Interestingly, the $[0\text{HS}:1\text{LS}]$ spin state displays symmetry breaking somewhere in the interval 90–85 K defining a high-symmetry phase at high temperature and another featuring low symmetry taking place at lower temperature. Irradiation of the low-symmetry $[0\text{HS}:1\text{LS}]$ phase with visible light at 15 K generates a low-symmetry $[1\text{HS}:0\text{LS}]^*$ phase, which differs from the heat-induced high-symmetry $[1\text{HS}:0\text{LS}]$ phase. The common feature between the distinct phases is the change in the angle defined by the two pyridine moieties of the 4,4'-bipy ligands. In this case, the competition between the orders (spin state vs structure) imposed by the spin state change and the 4,4'-bipy ligands is responsible for the multistability and the six crystallographic phases observed in 1bipy.^{7b} Furthermore, the Fe^{II} coordination site, surrounded by four equatorial SCN^- groups and two pyridine moieties, is as far as we know unprecedented in the SCO area.

The interesting properties shown by 1bipy motivated us to clarify whether the in situ formed $\{[\text{Hg}^{\text{II}}(\text{SCN})_4]_2(\mu\text{-}4,4'\text{-bipy})\}^{2-}$ bridges are fortuitous or, in contrast, it can be systematically synthesized to generate homologous 2D SCO-CPs using alternative ligands, L, with the same coordination topology of 4,4'-bipy. Here we report the synthesis, crystal structure, and magnetic and calorimetric studies of the compounds $\{\text{Fe}^{\text{II}}[\text{Hg}^{\text{II}}(\text{SCN})_4]_2(\text{L})_x\}_n \cdot \text{Solv}$, where $x = 2$ for $\text{L} = \text{tvp}$ (*trans*-(4,4'-vinylenedipyridine)) (1tvp), bpmh ((1*E*,2*E*)-1,2-bis(pyridin-4-yl)methylenediazine) (1bpmh·*n*CH₃OH), bpeh ((1*E*,2*E*)-1,2-bis(1-(pyridin-4-yl)ethylidenediazine) (1bpeh·*n*H₂O) and $x = 2.33$ for $\text{L} = \text{bpbz}$ ((1,4-bis(pyridin-4-yl)benzene)) (1bpbz·*n*H₂O) (see Scheme 1).

RESULTS

Synthesis. The title compounds were synthesized by slow diffusion methods using methanol–water solutions (see the Experimental Section for detailed information). Self-assembly of Fe^{II} , L, and $[\text{Hg}(\text{SCN})_4]^{2-}$ favors in situ generation of $\{[\text{Hg}(\text{SCN})_4]_2(\mu\text{-L})\}^{2-}$ species ($\text{L} = \text{tvp}, \text{bpeh}, \text{bpmh}, \text{bpbz}$) and subsequent formation of 2D coordination polymers

Scheme 1. Ligands Used in the Present Work



formulated as $\{\text{Fe}[\mu\text{-}(\text{Hg}(\text{SCN})_4)_2(\mu\text{-L})_2]\}$ (1L). Single-crystal X-ray analysis indicates that the derivative with tvp crystallizes without solvent molecules (1tvp), while the derivatives with $\text{L} = \text{bpeh}, \text{bpmh}, \text{bpbz}$ include 1 molecule of H₂O (1bpeh·H₂O), 1 molecule of CH₃OH (1bpmh·CH₃OH), and 2/3 molecule of H₂O (1bpbz·2/3H₂O) (vide infra). However, according to the thermal analysis (Figure S1 in the Supporting Information), these solvent molecules are labile and desorb when the crystals are not preserved, i.e. covered with oil or immersed in mother liquor, thereby affording the corresponding unsolvated forms (1bpeh, 1bpmh, 1bpbz). Simulated XRPD patterns from the solvated single-crystal structures compare reasonably well with those of the corresponding unsolvated experimental structures, indicating that the loss of the solvent molecules has little effect on the structure (Figures S2 and S3 in the Supporting Information).

Spin-Crossover Behavior. Magnetic Properties. The thermal dependence of the $\chi_M T$ product ($\chi_M =$ magnetic susceptibility, $T =$ temperature, scan temperature rate 1 K min⁻¹) for massive samples constituted of single crystals of 1bpbz, 1bpeh, 1tvp, and 1bpmh is shown in Figure 1a. In the interval 350–300 K, $\chi_M T$ is about 3.80–3.85 cm³ K mol⁻¹ for the four compounds, a value consistent with the Fe^{II} ion in the HS ($S = 2$) state. For 1bpmh, $\chi_M T$ remains practically constant upon cooling to 280 K. Then, $\chi_M T$ drops, reaching a value of 0.1 cm³ K mol⁻¹ at 150 K consistent with the Fe^{II} ion in the LS ($S = 0$) state. This behavior corresponds to a complete HS \leftrightarrow LS spin conversion characterized by the equilibrium temperature $T_{1/2} = 226$ K, at which the HS and LS molar fractions are equal to 0.5. The $\chi_M T$ vs T plots in the cooling and heating modes match perfectly, indicating the lack of thermal hysteresis. The magnetic behavior of 1tvp and 1bpeh is similar to that of 1bpmh but is shifted toward low temperatures. When the temperature is lowered, the SCO behavior starts just below 230 K and attains a value of 0.04 cm³ K mol⁻¹ at temperatures below 125 K for 1tvp. This complete SCO is characterized by $T_{1/2} = 177$ K. For 1bpeh the SCO starts at temperatures slightly lower than 180 K (cooling mode) and extends down to 100 K. Just below 100 K the slope of the SCO profile decreases slightly, most probably due to kinetic effects. At temperatures below 60 K, $\chi_M T$ attains a constant value of 0.59 cm³ K mol⁻¹, indicating that ca. 15% of Fe^{II} centers remain “frozen” in the HS state, most likely due to slowing of the HS \leftrightarrow LS conversion rate. An estimated value of $T_{1/2} = 119$ K can be obtained by considering a complete SCO as in the previous examples.

The magnetic behavior of 1bpbz features an incomplete SCO with 50% of Fe^{II} centers blocked in the HS ($\chi_M T = 1.82$ cm³ K mol⁻¹) at temperatures below 70 K. Consequently, we

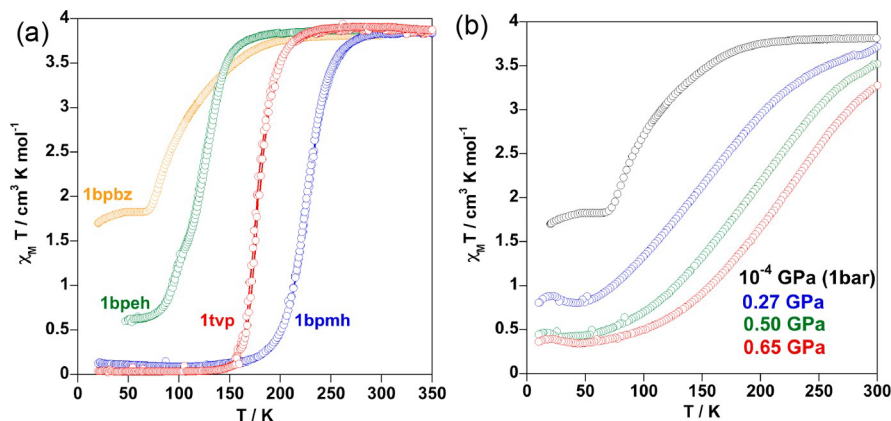


Figure 1. (a) $\chi_M T$ vs T plot for the series of compounds investigated. (b) $\chi_M T$ vs T plot for 1bpbz at different pressures.

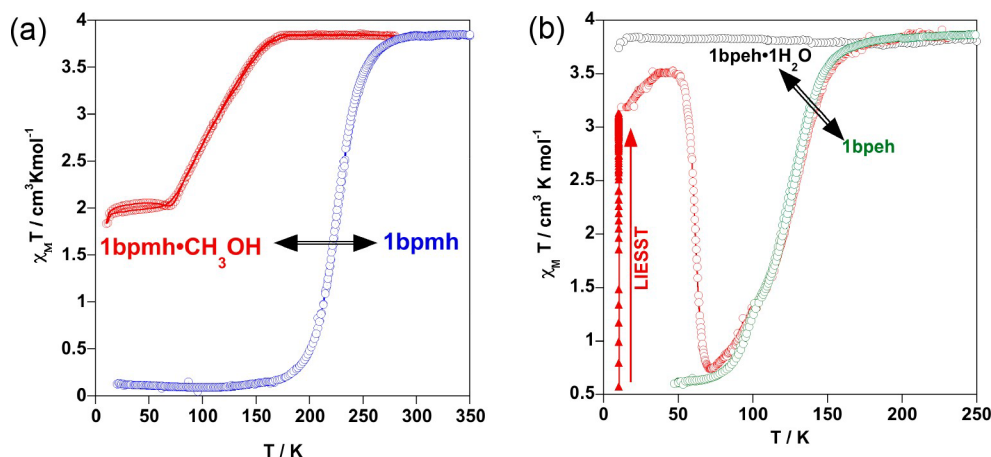


Figure 2. $\chi_M T$ vs T plots for (a) 1bpmh-CH₃OH (red) and its unsolvated form (blue) and (b) 1bpeh-H₂O (black), its unsolvated form 1bpeh (green), and the LIESST behavior of 1bpeh (red).

decided to investigate the evolution of the thermal dependence of $\chi_M T$ with pressure, more precisely at $p = 0.27, 0.50, 0.65$ GPa (see Figure 1b). Pressure makes the SCO more gradual but also more complete at low temperatures. The $T_{1/2}(p)$ values equaling 137 K (0.27 GPa), 186 K (0.50 GPa), and 216 K (0.65 GPa) were estimated from the $\chi_M T$ value associated with 50% transformation of the hypothetical complete SCO expected for 1bpbz: i.e. $(\chi_M T)_{T_{1/2}} \approx [(\chi_M T)_{\text{HS}} - (\chi_M T)_{\text{LS}}]/2$ with $(\chi_M T)_{\text{HS}} = 3.80 \text{ cm}^3 \text{ K mol}^{-1}$ and $(\chi_M T)_{\text{LS}} \approx 0 \text{ cm}^3 \text{ K mol}^{-1}$. The $T_{1/2}(p)$ vs p plot follows a linear dependence (Figure S4 in the Supporting Information) expected in the mean field theory of phase transitions expressed by the Clapeyron relation

$$T_{1/2}(p) = T_{1/2} + p(\Delta V_{\text{HL}}/\Delta S_{\text{HL}})$$

in which $\Delta V_{\text{HL}}/\Delta S_{\text{HL}} = \partial T_{1/2}(p)/\partial p$ represents the average pressure dependence of $T_{1/2}(p)$ and ΔV_{HL} and ΔS_{HL} are respectively the change in volume and entropy per mole of compound upon the SCO. A linear fitting of the experimental data gives a slope of 208 K GPa⁻¹, which is very close to those observed for the mononuclear compounds [Fe(PM-Aza)₂(NCS)₂] (160 K GPa⁻¹),⁹ [Fe(phen)₂(NCS)₂] (220 K GPa⁻¹) (phen = 1,10-phenanthroline),⁹ and [Fe(dpa)₂(NCS)₂] (187.5 K GPa⁻¹) (dpa = 2,2-dipyridylamine)¹⁰ and the 2D framework [Fe(dpms)₂(NCS)₂] (208 K GPa⁻¹) (dpms = 4,4'-dipyridylmethyl sulfide).¹¹

As mentioned above, the as-synthesized crystals of 1bpmh, 1bpeh, and 1bpbz include labile molecules of methanol (1bpmh-CH₃OH) and water (1bpeh-H₂O and 1bpbz-2/3H₂O) that persist while the crystals are protected. Aiming at investigating the effect of the inclusion on the SCO, we measured the magnetic properties of the three samples soaked in the mother liquor. Under these conditions, 1bpmh-CH₃OH shows typical $\chi_M T$ values of the HS state down to ca. 170 K. Then, below this temperature $\chi_M T$ decreases, describing a poor cooperative HS ↔ LS conversion that ends at ca. 70 K involving 50% of the Fe^{II} centers (see Figure 2a). Along the same line, the thermal dependence of $\chi_M T$ for the single crystals of 1bpeh-H₂O resulted to be HS at all temperatures (see Figure 2b). In contrast, 1bpbz-*n*H₂O displays the same SCO properties whatever the hydration degree, $n = 0$ or $n = 2/3$.

Photogeneration of the metastable HS* state at low temperature, the so-called light-induced excited spin state trapping (LIESST)¹² experiment, was carried out on a microcrystalline sample (2.70 mg) of 1bpeh (Figure 2b). The sample was cooled to 10 K, where $\chi_M T \approx 0.54 \text{ cm}^3 \text{ K mol}^{-1}$, and then it was irradiated with red light ($\lambda = 633 \text{ nm}$), thus attaining rapidly (less than 30 min) a $\chi_M T$ saturation value of ca. $3.11 \text{ cm}^3 \text{ K mol}^{-1}$. Afterward, light irradiation was switched off and the temperature increased at a rate of 0.3 K min⁻¹. In the range of temperature 10–38 K, $\chi_M T$ increases up to a maximum value of ca. $3.51 \text{ cm}^3 \text{ K mol}^{-1}$ at 36 K, reflecting the thermal population of the microstates arising from the zero-

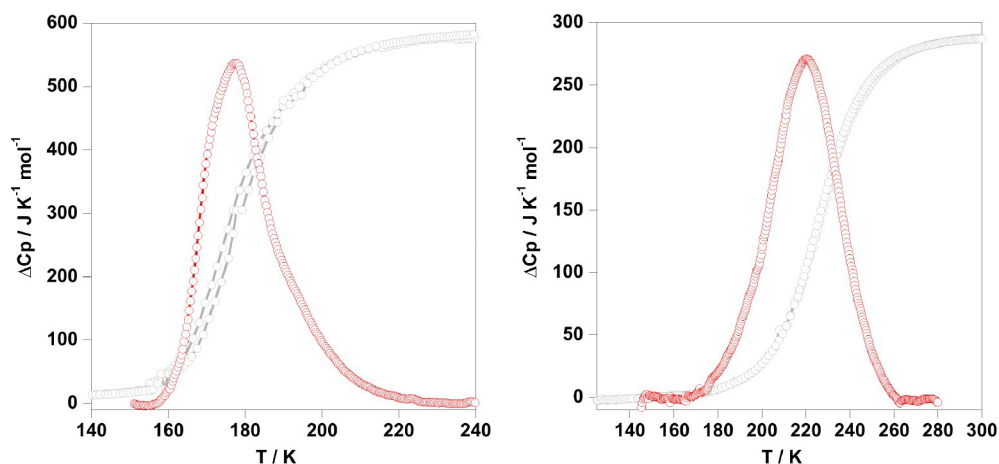


Figure 3. Overlay of the DSC (red) and magnetic (gray) curves for 1tvp (left) and 1bpmh (right).

Table 1. Crystallographic Parameters

	1tvp		1bpmh·CH ₃ OH 120 K	1bpeh·H ₂ O 250 K	1bpbz·2/3H ₂ O 293 K
	250 K	120 K			
empirical formula	C ₃₀ H ₂₀ FeHg ₂ N ₁₀ S ₆		C ₃₁ H ₂₄ FeHg ₂ N ₁₄ S ₆ O	C ₃₄ H ₃₀ FeHg ₂ N ₁₄ S ₆ O	C ₆₅ H ₄₂ Fe _{1.5} Hg ₃ N ₁₆ S ₉ O
<i>M_r</i>	1169.95		1258.03	1300.11	2037.23
cryst syst			triclinic		
space group			<i>P</i> $\bar{1}$		
<i>a</i> (Å)	8.7876(7)	8.5492(6)	8.6292(5)	8.4215(2)	12.7560(3)
<i>b</i> (Å)	8.9182(9)	8.8679(6)	8.9430(6)	9.6787(3)	15.8100(4)
<i>c</i> (Å)	13.718(2)	13.3905(9)	14.9860(9)	15.2108(5)	19.5190(4)
α (deg)	102.829(9)	75.629(6)	104.662(5)	101.391(3)	80.9970(10)
β (deg)	108.643(9)	73.551(6)	102.307(5)	103.457(2)	74.6390(10)
γ (deg)	92.201(7)	89.109(5)	92.415(5)	91.019(2)	69.3200(10)
<i>V</i> (Å ³)	986.2(2)	941.53(12)	1087.45(12)	1179.38(6)	3542.59(14)
<i>Z</i>			1		2
<i>D_c</i> (mg cm ⁻³)	1.970	2.063	1.921	1.831	1.908
μ (Mo K α) (mm ⁻¹)	8.480	8.883	7.702	7.108	7.099
<i>F</i> (000)	552	552	598	622	1946
total no. of rflns (<i>I</i> > 2 σ (<i>I</i>))	2949	3024	3161	3711	9393
<i>R</i> (<i>I</i> > 2 σ (<i>I</i>))	0.0340	0.0308	0.0598	0.0315	0.0417
<i>R</i> (all data)	0.0443	0.0350	0.0756	0.0369	0.0635
<i>S</i>	1.034	1.053	1.046	1.090	1.031

field splitting characteristic of the HS* (*S* = 2) state, and suggests that the light-induced population of this state is rather complete at 10 K. At temperatures greater than 50 K, $\chi_M T$ drops rapidly, attaining a value of about 0.74 cm³ K mol⁻¹ at ca. 72 K, which suggests a practically complete HS* \rightarrow LS relaxation to the initial $\chi_M T$ value. The *T*_{LIESST} value¹³ determined from the maximum variation of $\chi_M T$ in the HS \rightarrow LS relaxation is 61 K. Under the same working conditions the derivatives 1tvp and 1bpmh do not exhibit remarkable photomagnetic properties.

Calorimetric Properties. Differential scanning calorimetry (DSC) measurements were carried out for 1tvp and 1bpmh. The corresponding anomalous variation of the heat capacity ΔC_p vs *T* plots is depicted in Figure 3. The range of temperatures at which the SCO of 1bpeh takes place prevented us from monitoring its calorimetric properties. The critical temperatures obtained from the maximum of the ΔC_p vs *T* plots, *T*_{1/2} = 177 K (1tvp) and 220 K (1bpmh), reproduce those obtained from the magnetic data. The average enthalpy and entropy variations associated with the cooling and heating modes are ΔH = 10.5 kJ mol⁻¹ and ΔS = 48.0 J K⁻¹ mol⁻¹ for

1bpmh and ΔH = 12.3 kJ mol⁻¹ and ΔS = 69.4 J K⁻¹ mol⁻¹ for 1tvp. These values are in line with those typically found for most octahedral Fe^{II} complexes experiencing a more or less cooperative *S* = 2 \leftrightarrow *S* = 0 spin state change.¹⁴

Structural Analysis. Single crystals of the title compounds were picked out from the mother liquor, coated with high-viscosity oil, and placed in the goniometer at the appropriate temperature. The title compounds crystallize in the space group *P* $\bar{1}$ (triclinic crystal system). The crystal structure of 1tvp was analyzed at 250 and 120 K where, respectively, the HS and LS states are fully populated. Due to desorption of methanol in 1bpmh·CH₃OH, good-quality data have only been obtained at 120 K. The crystal structure was analyzed at 250 K for 1bpeh·H₂O and at 293 K for 1bpbz·2/3H₂O. Table 1 contains

relevant crystallographic data of the title compounds. Table 2 gathers the metal–ligand bond lengths, including the corresponding average value for the Fe centers ($\langle \text{Fe–N} \rangle$) and the angular distortion parameters \sum^{Fe} and \sum^{Hg} . The last two parameters correspond to the sum of deviations from the ideal octahedron/tetrahedron of the 12/6 “cis” bond angles

Table 2. Selected Bond Lengths (Å) and \sum^{Fe} and \sum^{Hg} (deg) Values (deg)

	1tvp		1bpmh-CH ₃ OH 120 K	1bpeh-H ₂ O 250 K	1bpbz-2/3H ₂ O 293 K			
	120 K	250 K			Fe1-N1		Hg1-S1	
Fe-N1	1.928(5)	2.135(5)	2.073(8)	2.141(6)	2.101(5)		Hg1-S1	2.616(2)
Fe-N2	1.939(5)	2.155(5)	2.083(8)	2.175(5)	2.172(5)		Hg1-S2	2.501(2)
Fe-N4	2.005(5)	2.187(4)	2.161(8)	2.197(5)	2.150(6)		Hg1-S9	2.457(3)
⟨Fe-N⟩	1.957(5)	2.159(5)	2.106(8)	2.171(6)	2.162(5)		Hg1-S9A	2.44(2)
\sum^{Fe}	4.12	13.20	16.8	23.0	2.197(5)		Hg1-N14	2.368(5)
					2.221(5)		Hg2-S4	2.521(2)
Hg-N5	2.398(5)	2.407(6)	2.419(10)	2.381(5)	2.154(5)		Hg2-S5	2.572(2)
Hg-S1	2.5533(16)	2.5323(19)	2.522(3)	2.577(2)	2.203(5)		Hg2-S6	2.417(3)
Hg-S2	2.5221(14)	2.5296(19)	2.532(3)	2.512(2)	2.174(5)		Hg2-S6A	2.483(12)
Hg-S3	2.4436(17)	2.424(2)	2.438(9)	2.398(3)	⟨Fe-N⟩	2.167/2.177	Hg2-N9	2.405(6)
Hg-S3A			2.459(10)		\sum^{Fe}	29.0/18.5	Hg3-S3	2.565(2)
\sum^{Hg}	72.8	73.8	80.8	65.3			Hg3-S7	2.523(2)
							Hg3-S8	2.458(5)
							Hg3-S8A	2.431(5)
							Hg3-N10	2.381(6)
							\sum^{Hg}	48.8/67.5/78.8°

($\sum^{Fe} = \sum_{i=1}^{12} |\theta_i - 90^\circ|$ and $\sum^{Hg} = \sum_{i=1}^6 |\theta_i - 109.5^\circ|$), respectively.

Structure of 1L-Solv [L = tvp, bpmh (Solv = CH₃OH) and bpeh (Solv = H₂O)]. The crystal structures of these three derivatives can be described in the same terms. They are characterized by the presence of three inversion centers: one lies on the Fe^{II} site, and the other two are located at the middle of the ethylene (tvp) or hydrazine (bpmh and bpeh) group of the two crystallographically unique L ligands. The Fe^{II} site defines a slightly elongated octahedron with the axial positions occupied by one of the two independent L ligands, while the equatorial positions are occupied by the nitrogen atoms of two crystallographically independent SCN⁻ groups (Figure 4a-c).

The almost planar L ligands, axially coordinated to the Fe^{II} centers, act as bridges defining [Fe(μ -L)]_n²ⁿ⁺ chains running along [001], while two practically linear and independent thiocyanate groups radiate from the Fe centers along the [100] and [010] directions. Both thiocyanate groups also belong to the in situ generated centrosymmetric {[Hg^{II}(SCN)₃]₂(μ -L)}²⁻ dimeric units constituted of two distorted-tetrahedral [Hg^{II}S₃N] coordination sites. Each tetrahedron is completed with the S atom of an almost linear terminal thiocyanate group and the N atom of the second crystallographically unique centrosymmetric L ligand (Figure 4d-f). The terminal SCN⁻ group of the 1bpmh-CH₃OH (S3-C3-N3) and 1bpeh-H₂O (S3-C3-N3) derivatives is strongly disordered.

For 1tvp, the ⟨Fe-N⟩ values 1.957(5) (120 K) and 2.159(5) Å (250 K) are consistent with the Fe^{II} centers in the LS and HS states, respectively. Indeed, the difference between these average bond lengths, 0.20 Å, indicates that the LS ↔ HS conversion is complete, according to the magnetic behavior. As expected, the \sum^{Fe} parameter is larger in the HS state, 13.20°, and decreases considerably in the LS state, 4.12°. Favored by the monodentate nature of the ligands involved in these compounds, the \sum^{Fe} parameters are consistent with the quasi-regular octahedral geometry (particularly in the LS Fe^{II} ion) of the title compounds.

The average ⟨Fe-N⟩ bond length, 2.106(8) Å for 1bpmh-CH₃OH and 2.171(6) Å for 1bpeh-H₂O, are respectively 0.053 Å smaller and 0.012 Å larger than those observed for 1tvp in the HS state. The ⟨Fe-N⟩ value found for 1bpmh-CH₃OH

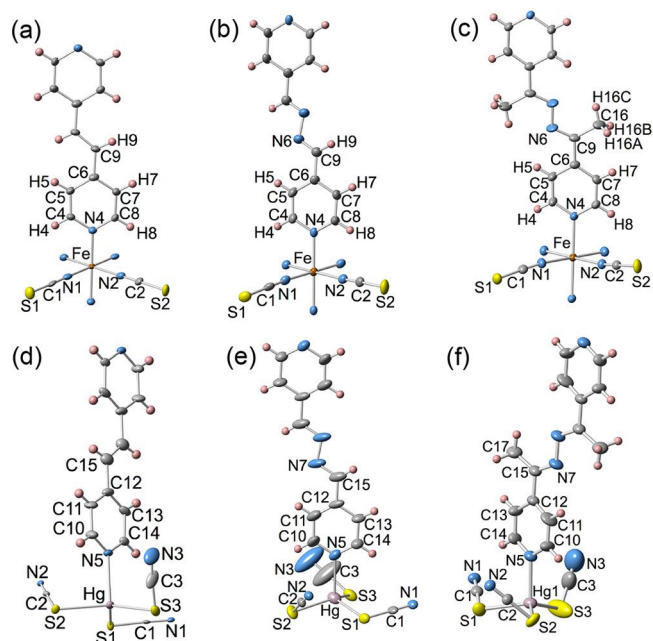


Figure 4. ORTEP representation of the Fe^{II} and Hg^{II} sites for 1tvp (a, d), 1bpmh-CH₃OH (b, e), and 1bpeh-H₂O (c, f), respectively, and atom numbering of the asymmetric units. Thermal ellipsoids are at 50% level for the Fe^{II} sites and at 30% for the Hg^{II} sites. For the sake of simplicity only one atomic position of the disordered S3-C3-N3 moieties is shown.

indicates that the structure contains a HS:LS mixture of Fe^{II} spin states of ca. 75:25 at 120 K, in agreement with the magnetic measurements performed in the presence of the mother liquid. In contrast, the ⟨Fe-N⟩ value found for 1bpeh-H₂O at 250 K is consistent with the fully populated HS state of Fe^{II}, as is also reflected by the magnetic data. Accordingly, the \sum^{Fe} parameter is consistent with the HS population of the last two compounds.

The [Hg^{II}S₃N] coordination core is quite the same in the three derivatives (Table 2). The coordination geometry is highly distorted with respect to the ideal tetrahedron. Indeed, the angular parameter \sum^{Hg} is in the range 66–79°. In all cases,

the NCS⁻ groups are strongly tilted with respect to the Hg–S bond, defining Hg–SCN angles in the interval 90–100°. The LS and HS structures of 1tvp show that the geometry of the [Hg^{II}S₃N] core is not significantly affected by a change in the spin state of the Fe^{II}.

The centrosymmetric dimeric units {[Hg^{II}(SCN)₃]₂(μ-L)}²⁻ act as bridges between adjacent [Fe(μ-L)]_n²ⁿ⁺ chains, thereby defining layers lying parallel to the (101) plane (Figure 5). The

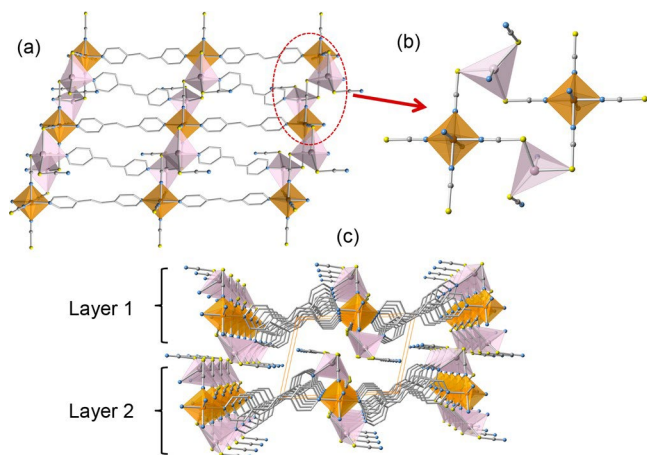


Figure 5. (a) Fragment of a layer displaying the [Fe(μ-tvp)]_n²ⁿ⁺ chains connected through {[Hg^{II}(SCN)₃]₂(μ-L)}²⁻ units. (b) View down the [001] direction of the connection between two chains (note that this connection contains another relevant inversion center). (c) Stack of two consecutive layers. Coordination centers: [FeN₆] (orange), [HgS₃N] (pink).

Fe^{II} atoms of a layer are perfectly coplanar, the separation between two consecutive planes being 8.633 Å (HS) (8.567 Å (LS)), 8.607 Å (75HS:25LS), and 9.467 Å (HS) for 1tvp, 1bpmh·CH₃OH, and 1bpeh·H₂O, respectively. As far as the crystal packing is concerned, there are small differences between the tvp and bpmh derivatives but the presence of the methyl groups (C16) in the bpeh derivative makes the packing less dense. Most likely, the larger separation between the pyridyl groups in the bpmh and bpeh derivatives favors the

inclusion of CH₃OH and H₂O, respectively (Figure S5 in the Supporting Information). No noticeable short contacts smaller than the sum of the van der Waals radii occur between adjacent layers. The molecules of MeOH in the bpmh derivative are organized in pairs, denoting the mutual interaction $d(O1\cdots O1) = 3.36(6)$ Å. Additionally, short contacts $O1\cdots C11$ (3.57(3) Å), $O1\cdots C11$ (3.19(4) Å), $O1\cdots C10$ (3.50(4) Å), $O1\cdots C7$ (3.50(4) Å), and $C16\cdots N7$ (3.47(3) Å) take place between the MeOH and its surroundings. In contrast, in the bpeh derivative the disordered H₂O molecule is well separated from the layers, thus reducing the number of significant intermolecular contacts ($O1\cdots C16$ (3.63(2) Å) and $O1\cdots N3$ (3.08(3) Å)).

Structure of 1bpbz·2/3H₂O. The crystal structure of this derivative is closely related to the structures described above. Nevertheless, there are some remarkable differences. For example, there are two distorted-octahedral [Fe^{II}N₆] centers (labeled Fe1, Fe2) segregated in alternate [Fe(μ-bpbz)]_n²ⁿ⁺ chains running along [010]. The chains defined by the Fe1 sites do not house any element of symmetry, while the chains defined by the Fe2 sites contain two inversion centers, one lying on the Fe2 site and the other on the center of the benzene ring of the bpbz ligand (Figure 6). The average bond lengths ⟨Fe–N⟩ = 2.167(6) (Fe1) and 2.177(6) Å (Fe2) as well as the angular distortion parameter $\sum^{Fe} = 29.0^\circ$ (Fe1) and 18.5° (Fe2) are consistent with the fully populated HS state displayed by this compound at temperatures above 200 K, in agreement with the magnetic data. In addition, there are three crystallographically distinct [Hg^{II}S₃N] coordination cores (labeled Hg1–3). The Hg1 site defines terminal [Hg(SCN)₃(bpbz)]⁻ units instead of dinuclear {[Hg^{II}(SCN)₃]₂(μ-bpbz)}²⁻ bridges. In contrast, Hg2 and Hg3 are connected by the same bpbz ligand defining a noncentrosymmetric dinuclear bridging unit (Figure 7). The metric parameters of the Hg sites are similar to those found for the other members of this series of compounds (Table 2). The presence of the terminal [Hg(SCN)₃(bpbz)]⁻ generates a kind of “defect” in the structure of the layers, since the sequence ***ABAB*** of parallel [Fe(μ-bpbz)]_n²ⁿ⁺ chains connected through the dinuclear {[Hg(2,3)(SCN)₃]₂(μ-bpbz)}²⁻ bridges is periodically interrupted, giving ***Fe1Fe2Fe1*** triads separated by two terminal [Hg1-

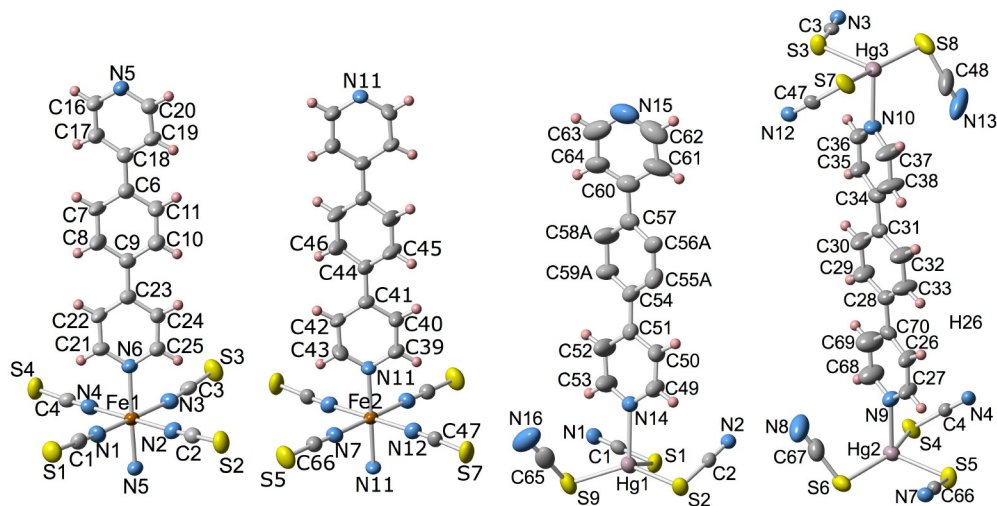


Figure 6. ORTEP representation of the Fe^{II} and Hg^{II} sites for 1bpbz·2/3H₂O and atom numbering of the asymmetric units. Thermal ellipsoids are at the 50% level for the Fe^{II} sites and at the 40% level for the Hg^{II} sites. For the sake of simplicity only one atomic position of the disordered terminal SCN moieties is shown.

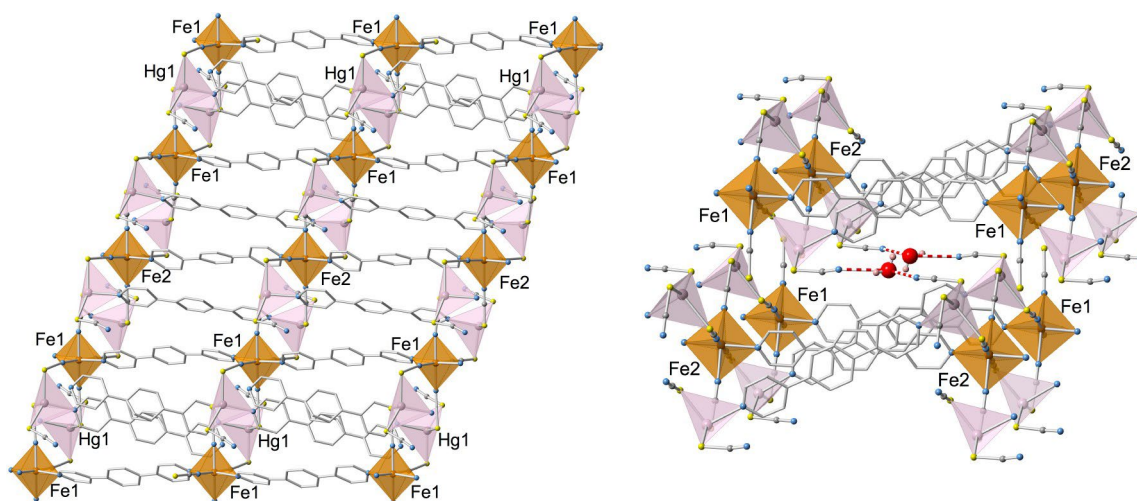


Figure 7. Fragment of a layer displaying sequences Fe1***Fe2***Fe1 of $[\text{Fe}(\mu\text{-bpbz})]_n^{2n+}$ chains separated by terminal pairs of $\{\text{Hg}^{\text{II}}(\text{SCN})_3\}_2(\text{bpbz})^-$ moieties (left). Stacking of two consecutive layers showing the included water molecule and its interactions with the N atom of the terminal NCS moieties (right).

$(\text{SCN})_3(\text{bpbz})^-$ units in which the bpbz units are turned ca. 90° with respect to the bridging bpbz ligands (Figure 7, left). Between the layers there are included water molecules, which display strong hydrogen-bond interactions with the N13 and N8 atoms of two terminal SCN^- groups belonging to the Hg3 and Hg2 centers of two consecutive layers (Figure 7, right). The $\text{O1}^{\cdots}\text{N13}$ and $\text{O1}^{\cdots}\text{N8}$ lengths are 2.97(2) and 2.887(15) Å, respectively. The separation between atoms belonging to two consecutive layers is 9.023(14) Å.

CONCLUDING REMARKS

The results here reported confirm that self-assembly of Fe^{II} , $[\text{Hg}(\text{SCN})_4]^{2-}$, and rodlike bis-monodentate ligands $L = 4,4'$ -bipy, tvp, bpmh, bpeh, bpbz containing 4-substituted pyridyl donor groups favors the formation of dinuclear species $\{[\text{Hg}^{\text{II}}(\text{SCN})_3]_2(\mu\text{-L})\}^{2-}$, which in turn act as linkers between linear $[\text{Fe}(\mu\text{-L})]_n^{2n+}$ chains, thus generating highly crystalline 2D CPs in good yield. This series of 2D CPs illustrates how sensitive the SCO behavior is to relatively small structural modifications. Indeed, the tvp, bpmh, bpeh, and bpbz bridging ligands change drastically the correlation between the elastic interactions and mechanical frustration, responsible for the generation of HS and LS long-range order in the 4,4'-bipy derivative.⁷ Therefore, for the new members of the series the SCO behavior occurs practically in one step without symmetry breaking,⁸ thus generating usually observed homogeneous LS or HS phases at low and high temperatures, respectively.

The equilibrium temperatures, $T_{1/2}$, estimated for the series (<70 K (1bpbz), 119 K (1bipy), 119 K (1bpeh), 177 K (1tvp) and 226 K (1bpmh)) seems not to have an obvious rationalization. The bridging ligands coordinated to the Fe^{II} centers afford similar donor groups, although they differ in length and flexibility. For example, the ligand field strength felt by the Fe^{II} centers in 1bpeh is virtually the same as that generated by the ligand 4,4'-bipy in 1bipy, despite the obvious differences in length and rigidity between bpeh and 4,4'-bipy. In contrast, the closely related bpmh and bpeh ligands should afford very similar SCO properties; however, the LS state of 1bpmh is about 107 K more stabilized than the LS state of 1bpeh. This marked difference in $T_{1/2}$ might reflect small changes in the packing of the layers due to steric perturbation

caused by the methyl groups in the bpeh derivative. This conjecture is in line with the large differences observed in the SCO behavior on moving from the solvated (1bpmh· CH_3OH and 1bpeh· H_2O) to the unsolvated (1bpmh and 1bpeh) forms. The presence of methanol/water molecules between the layers provokes a drastic decrease in $T_{1/2}$ of more than 100 K. Thus, 1bpmh· CH_3OH undergoes a 50% HS \leftrightarrow LS conversion at very low temperatures (Figure 2a), while the HS \leftrightarrow LS conversion is completely inhibited in the case of 1bpeh· H_2O (Figure 2b). The solvent inclusion stabilizes the HS state in both compounds. In 1bpmh· CH_3OH , the oxygen atom of the methanol molecule displays short $\text{O}^{\cdots}\text{C}$ contacts with some carbon atoms of the pyridine moieties coordinated to the Hg^{II} ($\text{O1}^{\cdots}\text{C11}$ and $\text{O1}^{\cdots}\text{C10}$) and Fe^{II} ($\text{O1}^{\cdots}\text{C7}$) centers. These intermolecular interactions seem to induce subtle structural and electronic constraints responsible for the observed decrease of effective ligand field strength in the Fe centers. The small differences observed in the XRPD patterns on both solvated and unsolvated forms could tentatively be attributed to reaccommodation of the 2D layers. This reasoning should also be valid for 1bpeh· H_2O , although the number of short contacts between the disordered water molecule and its surroundings is smaller. In both cases, the lack of structural analysis for the unsolvated form precludes us from providing more precise information.

Conversely, the SCO behavior in 1bpbz· $n\text{H}_2\text{O}$ is essentially the same whatever the degree of solvation, $n = 0$ or $n = 2/3$, and resembles the SCO of 1bpmh· CH_3OH . On one hand, this insensitiveness of the SCO to the degree of solvation may be related to the more rigid nature of the bpbz ligand and hence of the 2D layers defined by 1bpbz· $n\text{H}_2\text{O}$. On the other hand, the incomplete nature of the SCO is most likely related to the weaker ligand field generated by bpbz. In this respect, the rigid bpbz ligand can be seen as an extension of the 4,4'-bipyridine ligand. In the 1bipy complex the SCO takes place in three well-defined SCO steps.⁷ A first HS \rightarrow LS step, involving 50% conversion, occurs over a wide interval of temperatures (170–125 K) and defines an ordered [1HS:1LS] state, which is stable down to 108 K. However, the two subsequent steeper steps occur in the low-temperature interval 108–96 K. One step defines an incommensurate [1HS:2LS] state, and the other

corresponds to the ordered [OHS:1LS] state. The 50% SCO behavior displayed by 1bpbz·*n*H₂O could be assimilated to the first step observed for 1bipy but shifted to slightly lower temperatures. Given that this step extends down to 70 K, further transformation to the LS spin state of the remaining 50% HS centers in 1bpbz·*n*H₂O gets kinetically frozen in. These features suggest that the ligand field induced by bpbz in 1bpbz·*n*H₂O is slightly smaller than that generated by 4,4'-bipyridine in 1bipy.

The LIESST effect was investigated for 1bpeh, 1tvp, and 1bpmh. The last two compounds are insensitive to the usual green or red light sources, while 1bpeh exhibits a complete LS → HS transformation characterized by $T_{\text{LIESST}} = 61$ K. This value is consistent with $T_{\text{LIESST}} = 54$ K previously reported for 1bipy. T_{LIESST} denotes the thermal stability of the photo-generated metastable HS state, and it has been correlated with $T_{1/2}$ through the expression $T_{\text{LIESST}} = T_0 - 0.3T_{1/2}$, where T_0 is a parameter that depends, in an imprecise way, on the nature of the ligands coordinated to Fe^{II}, distortion of the coordination octahedron, dimensionality of the complex, etc.¹³ When the values $T_{1/2}$ and T_{LIESST} experimentally obtained for 1bpeh and 1bipy are introduced in the aforementioned correlation, a T_0 value in the interval 90–100 K is estimated. Assuming that this T_0 value is also valid for 1tvp and 1bpmh, the corresponding estimated T_{LIESST} values are equal to 46.9 and 32.2 K, respectively. Given that the experimental $T_{1/2}$ values of the latter compounds are much larger than those of 1bpeh and 1bipy, these T_{LIESST} temperatures are consistently smaller than the experimental temperature observed for 1bpeh and 1bipy but are much larger than those expected, since 1tvp and 1bpmh do not exhibit LIESST. The thermal instability of the photogenerated HS state in the last two compounds can be explained in part by their high $T_{1/2}$ values and probably by subtle structural differences that determine T_0 values in the

interval 70–80 K. In this respect, it deserves emphasizing that we are dealing with a series of unprecedented bimetallic SCO-CPs and that despite the number of SCO-CPs being very large only very few of them display a LIESST effect and consequently the number of reported T_{LIESST} values for SCO-CPs is extremely limited.¹⁵

It is worth comparing the title compounds 1bipy, 1tvp, and 1bpmh with the series of 2D SCO-CPs generically formulated [Fe(L)₂(NCS)₂]ⁿGuest, L = 4,4'-bipy,¹⁶ tvp,¹⁷ bpmh.¹⁸ In the latter compounds the nearest coordination sphere of the Fe^{II} can be described as the reverse of that of the title compounds 1bipy, 1tvp, and 1bpmh: namely, the axial positions are occupied by two SCN⁻ groups while the four bridging 4,4'-bipy, tvp, or bpmh ligands occupy the equatorial positions linking adjacent Fe^{II} atoms, thereby defining 2D grid-layered CPs. Interestingly, the nature of the L ligand determines the supramolecular organization of the [Fe(L)₂(NCS)₂] layers in the crystal: i.e., different kinds of parallel stacks as well as parallel or inclined interpenetration. The guests are located in the channels defined by the layers and seem to convey some rigidity and/or chemical pressure to the structure, which is presumably required for the occurrence of SCO. Given that the “SCN” moiety induces a weaker ligand field in comparison to the pyridyl moiety on the Fe^{II}, one should expect much lower critical temperatures for 1bipy, 1tvp, and 1bpmh than for their [Fe(L)₂(NCS)₂]ⁿGuest counterparts. However, the experimental results do not support this conjecture. Indeed, the magnitude of $T_{1/2}$ for 1bipy and 1tvp is similar to that of [Fe(4,4'-bipy)₂(NCS)₂]ⁿ4CHCl₃ and [Fe(tvp)₂(NCS)₂]ⁿ

*n*Guest (*n*Guest = 1CH₃OH, 2C₆H₅CHO, 4(CH₃CN·H₂O), 2((CH₃)₂SO), etc.), respectively.^{16,17b} A possible explanation for this observation could be related to the more robust/rigid nature and denser packing of the 2D layers in the {Fe^{II}[(Hg^{II}(SCN)₃]₂(L)₂} system. Indeed, each dimeric {[Hg^{II}(SCN)₃]₂(μ-L)}²⁻ rigid linker acts as a tetratopic unit connecting 4 Fe^{II} centers belonging to adjacent [Fe(μ-L)]_n²ⁿ⁺ chains. Although it is topologically comparable to the bridging aptitude of the mononuclear metalloligands [M^{II}(CN)₄]²⁻ (M^{II} = Ni, Pd, Pt), the situation in which a polynuclear center acts as a secondary building unit is uncommon in SCO-PCs. Furthermore, the dense packing between the layers is in some cases adverse to the inclusion of solvent (1bipy, 1tvp), although in the case of 1bpmh·CH₃OH and 1bpeh·H₂O the length and shape of the ligand favors the formation of small pockets where the solvent molecules are loosely attached. In contrast to the [Fe(L)₂(NCS)₂]ⁿGuest series, the influence of these guest molecules has a negative impact on their SCO behavior.

In summary, the results here reported consolidate an unprecedented family of thiocyanate-based heterobimetallic Fe^{II}–Hg^{II} 2D SCO-CPs. The principle of construction requires self-assembly of bis-monodentate rodlike ligands (L) containing 4-pyridyl moieties, Fe^{II}, and [Hg^{II}(SCN)₄]²⁻. This favors the generation of dimeric tetratopic secondary building units {[Hg^{II}(SCN)₃]₂(μ-L)}²⁻ whose peripheral SCN⁻ groups link [Fe(μ-L)]_n²ⁿ⁺ chains. This situation strongly contrasts with our preliminary results based on the 3,3'-bipyridine ligand, which affords the complex {Fe^{II}(3,3'-bipyridine)[Hg^{II}(CN)₄]_n. This result suggests that the use of 3-pyridyl moieties does not favor the generation of dimeric secondary building units. Indeed, in the latter compound, the resulting zigzag [Fe(μ-3,3'-bipyridine)]_n²ⁿ⁺ chains are held together through the four SCN⁻ arms of the single [Hg(SCN)₄]₂₋ units, thereby affording a 3D coordination polymer, which remains HS at all temperatures (see Tables S1 and S2 and Figure S7 in the Supporting Information).

EXPERIMENTAL SECTION

Materials. All precursor reagents were obtained from commercial sources. The ligands bpmh, bpeh, and bpbz were synthesized following the synthetic procedures previously reported.^{18,19}

Synthesis. Compound 1 was obtained by diffusion in three-arm H-type vessels. One arm of the vessel contained an aqueous solution (0.5 mL) of FeCl₂ (0.10 mmol, 12.7 mg), while the middle arm contained a water solution of K₂[Hg(SCN)₄] (0.5 mL) prepared in situ by mixing Hg(SCN)₂ (0.1 mmol) and KSCN (0.2 mmol). The other arm of the vessel contained a methanol solution (0.5 mL) of tvp (0.10 mmol, 18.2 mg), bpmh (0.10 mmol, 21.0 mg), bpeh (0.10 mmol, 23.8 mg), or bpbz (0.10 mmol, 23.2 mg). The three arms were filled with methanol, sealed, and left in a quiet place. Light orange blocklike crystals of 1tvp, 1bpmh·CH₃OH, 1bpeh·H₂O, and 1bpbz·2/3H₂O suitable for single-crystal X-ray analysis were obtained after about 1 week (yield ca. 50%). The most striking feature of the IR spectrum is an intense multiple band with peaks and less intense shoulders in the intervals 2142–2116 and 2095–2045 cm⁻¹, respectively, which correspond to the ν(CN) stretching modes of the distinct NCS⁻ groups (Figure S6 in the Supporting Information). Anal. Found for 1tvp: C, 29.39; H, 1.66; N, 11.51. Calcd for C₃₀H₂₆FeHg₂N₁₀S₆: C, 30.80; H, 1.72; N, 11.97. Anal. Found for 1bpmh: C, 29.13; H, 1.74; N, 15.81. Calcd for C₃₁H₂₄FeHg₂N₁₄OS₆: C, 29.39; H, 1.64; N, 16.00. Anal. Found for 1bpeh: C, 31.29; H, 2.23; N, 15.06. Calcd for C₃₄H₂₈FeHg₂N₁₄S₆: C, 31.85; H, 2.20; N, 15.30. Anal. Found for 1bpbz: C, 38.23; H, 2.11; N, 10.97. Calcd for C₆₅H₄₂Fe₁₅Hg₃N₁₆S₉: C, 38.62; H, 2.08; N, 11.09.

Physical Measurements. Variable-temperature magnetic susceptibility data were recorded with a Quantum Design MPMS2 SQUID magnetometer equipped with a 7 T magnet, operating at 1 T and at temperatures of 1.8–400 K. Magnetic measurements under pressure were performed on 1bpbz using a hydrostatic pressure cell made of hardened beryllium bronze with silicon oil as the pressure-transmitting medium operating over the pressure range 1 bar to 10 kbar. The compound (10 mg) was packed in a cylindrically shaped sample holder (1 mm in diameter and 5–7 mm in length) made up of very thin aluminum foil. The pressure was calibrated using the transition temperature of superconducting high-purity 99.999% lead. Experimental susceptibilities were corrected for diamagnetism of the constituent atoms by the use of Pascal's constants. Calorimetric measurements were performed using a Mettler Toledo DSC 821e differential scanning calorimeter. Low temperatures were obtained with an aluminum block attached to the sample holder, refrigerated with a flow of liquid nitrogen, and stabilized at a temperature of 110 K. The sample holder was kept in a drybox under a flow of dry nitrogen gas to avoid water condensation. The measurements were carried out using around 15 mg of microcrystalline samples of 1tvp and 1bpmh sealed in aluminum pans with a mechanical crimp. Temperature and heat flow calibrations were made with standard samples of indium by using its melting transition (429.6 K, 28.45 J g⁻¹). An overall accuracy of ±0.2 K in temperature and ±2% in the heat capacity is estimated. The uncertainty increases for the determination of the anomalous enthalpy and entropy due to the subtraction of an unknown baseline. Powder X-ray measurements were performed on a PANalytical Empyrean X-ray powder diffractometer (monochromatic Cu K α radiation).

Single-Crystal X-ray Diffraction. Single-crystal X-ray data were collected on an Oxford Diffraction Supernova diffractometer using graphite-monochromated Mo K α radiation ($\lambda = 0.71073$ Å). A multiscan absorption correction was performed. The structures were solved by direct methods using SHELXS-2014 and refined by full-matrix least squares on F^2 using SHELXL-2014.²⁰ Non-hydrogen atoms were refined anisotropically, and hydrogen atoms were placed in calculated positions refined using idealized geometries (riding model) and assigned fixed isotropic displacement parameters.

Responses to the alerts of type A or B appearing in some title compounds are provided in the corresponding CIF file and are related to low diffraction intensity of the crystals. Nevertheless, the crystallographic data fully convey all the chemical and structural meaning required to explain correctly the structures and the spin crossover behavior in this series of compounds. Supplementary crystallographic CIF data (CCDC numbers: 1585093 (1tvp, low-spin); 1585094 (1tvp, high spin); 1585095 (1dpmh·CH₃OH); 1585096 (1bpeh·H₂O); 1585097 (1dpbz·2/3H₂O); 1585098 ({Fe-(3,3'-bipyrimidine)[Hg(SCN)₄]})) can be obtained free of charge from the Cambridge Crystallographic Data Centre.

ASSOCIATED CONTENT

AUTHOR INFORMATION

Corresponding Author

*E-mail for J.A.R.: jose.a.real@uv.es.

ORCID

José Antonio Real: 0000-0002-2302-561X

Notes

The authors declare no competing financial interest.

ACKNOWLEDGMENTS

We thank the Spanish Ministerio de Economía y Competitividad (MINECO), FEDER funds (CTQ2013-46275-P and CTQ2016-78341-P and Unidad de Excelencia María de Maeztu MDM-2015-0538), and Generalitat Valenciana (PROMETEO/2016/147). F.J.V.-M. thanks MINECO for a predoctoral FPI grant. D.Z. acknowledges support from the Natural Science Foundation of China (21671121).

REFERENCES

- (1) See for example: (a) Hauser, A. Intersystem Crossing in Iron(II) Coordination Compounds: A Model Process between Classical and Quantum Mechanical Behaviour. *Comments Inorg. Chem.* 1995, 17, 17–40. (b) König, E. Nature and Dynamics of the Spin-State Interconversion in Metal-Complexes. *Struct. Bonding (Berlin, Ger.)* 1991, 76, 51–152. (c) Gülich, P.; Hauser, A.; Spiering, H. Thermal and Optical Switching of Iron(II) Complexes. *Angew. Chem., Int. Ed. Engl.* 1994, 33, 2024–2054. (d) Sato, O. Optically Switchable Molecular Solids: Photoinduced Spin-Crossover, Photochromism, and Photoinduced Magnetization. *Acc. Chem. Res.* 2003, 36, 692–700. (e) Real, J. A.; Gaspar, A. B.; Niel, V.; Muñoz, M. C. Communication between Iron(II) Building Blocks in Cooperative Spin Transition Phenomena. *Coord. Chem. Rev.* 2003, 236, 121–141. (f) *Spin Crossover in Transition Metal Compounds I-III*; Gülich, P., Goodwin, H. A., Eds.; Springer: Berlin, 2004; Vols. 233–235. (g) Real, J. A.; Gaspar, A. B.; Muñoz, M. C. Thermal, Pressure and Light Switchable Spin-Crossover Materials. *Dalton Trans.* 2005, 2062–2079. (h) Halcrow, M. A. Iron(II) Complexes of 2,6-di(pyrazol-1-yl)pyridines A Versatile System for Spin-Crossover Research. *Coord. Chem. Rev.* 2009, 253, 2493–2514. (i) Olguin, J.; Brooker, S. Spin Crossover Active Iron(II) Complexes of Selected pyrazole-pyridine/pyrazine Ligands. *Coord. Chem. Rev.* 2011, 255, 203–240. (j) Bousseksou, A.; Molnár, G.; Salmon, L.; Nicolazzi, W. Molecular Spin Crossover Phenomenon: Recent Achievements and Prospects. *Chem. Soc. Rev.* 2011, 40, 3313–3335. (k) Halcrow, M. A. The Spin-States and Spin-Transitions of Mononuclear Iron(II) Complexes of Nitrogen-Donor Ligands. *Polyhedron* 2007, 26, 3523–3576.
- (2) (a) Meded, V.; Bagrets, A.; Fink, K.; Chandrasekar, R.; Ruben, M.; Evers, F.; Bernand-Mantel, A.; Seldenthuis, J. S.; Beukman, A.; van der Zant, H. S. J. Electrical Control over the Fe(II) Spin Crossover in a Single Molecule: Theory and Experiment. *Phys. Rev. B: Condens. Matter Mater. Phys.* 2011, 83, 245415. (b) Prins, F.; Monrabal-Capilla, M.; Osorio, E. A.; Coronado, E.; van der Zant, H. S. J. Room-Temperature Electrical Addressing of a Bistable Spin-Crossover Molecular System. *Adv. Mater.* 2011, 23, 1545–1549. (c) Cavallini, M.; Bergenti, I.; Milita, S.; Kengne, J. C.; Gentili, D.; Ruani, G.; Salitros, I.; Meded, V.; Ruben, M. Thin Deposits and Patterning of Room-Temperature-Switchable One-Dimensional Spin-Crossover Compounds. *Langmuir* 2011, 27, 4076–4081. (d) Miyamachi, T.; Gruber, M.; Davesne, V.; Bowen, M.; Boukari, S.; Joly, L.; Scheurer, F.

- Rogez, G.; Yamada, T. K.; Ohresser, P.; Beaurepaire, E.; Wulfhekel, W. Robust Spin Crossover and Memristance across a Single Molecule. *Nat. Commun.* 2012, 3, 938. (e) Martinho, P. N.; Rajnak, C.; Ruben, M. In *Spin-Crossover Materials: Properties and Applications*; Halcrow, M. A., Ed.; Wiley: Hoboken, NJ, 2013; pp 376–404, and references therein. (f) Shepherd, H. J.; Molnár, G.; Nicolazzi, W.; Salmon, L.; Bousseksou, A. Spin Crossover at the Nanometre Scale. *Eur. J. Inorg. Chem.* 2013, 2013, 653–661. (g) Rotaru, A.; Dugay, J.; Tan, R. P.; Gural'skiy, I. A.; Salmon, L.; Demont, P.; Carrey, J.; Molnár, G.; Respaud, M.; Bousseksou, A. Nano-Electromanipulation of Spin Crossover Nanorods: Towards Switchable Nanoelectronic Devices. *Adv. Mater.* 2013, 25, 1745–1749. (h) Gural'skiy, I. A.; Quintero, C. M.; Sanchez Costa, J.; Demont, P.; Molnár, G.; Salmon, L.; Shepherd, H. J.; Bousseksou, A. Spin Crossover Composite Materials for Electrothermomechanical Actuators. *J. Mater. Chem. C* 2014, 2, 2949–2955. (i) Bartual-Murgui, C.; Akou, A.; Thibault, C.; Molnár, G.; Vieu, C.; Salmon, L.; Bousseksou, A. Spin-Crossover Metal-Organic Frameworks: Promising Materials for Designing Gas Sensors. *J. Mater. Chem. C* 2015, 3, 1277–1285. (j) Aragonés A. C.; Aravena, D.; Cerda, J. I.; Acís-Castillo, Z.; Li, H.; Real, J. A.; Sanz, F.; Hihath, J.; Ruiz, E.; Díez-Pérez, I. Large Conductance Switching in a Single-Molecule Device through Room Temperature Spin-Dependent Transport. *Nano Lett.* 2016, 16, 218–226.
- (3) (a) García, Y.; Niel, V.; Muñoz, M. C.; Real, J. A. Spin crossover in 1D, 2D and 3D polymeric Fe(II) networks. *Top. Curr. Chem.* 2004, 233, 229–257. (b) Muñoz, M. C.; Real, J. A. Polymeric Spin-Crossover Materials. In *Spin-Crossover Materials: Properties and Applications*; Halcrow, M. A., Ed.; Wiley: Hoboken, NJ, 2013; pp 121–146.
- (4) (a) Muñoz, M. C.; Real, J. A. Thermo-, Piezo-, Photo- and Chemo-Switchable Spin Crossover Iron(II)-Metalloctyanate Based Coordination Polymers. *Coord. Chem. Rev.* 2011, 255, 2068–2093. (b) Ni, Z.-P.; Liu, J.-L.; Hoque, Md. N.; Liu, W.; Li, J.-Y.; Chen, Y.-C.; Tong, M.-L. Recent advances in guest effects on spin-crossover behavior in Hofmann-type metal-organic frameworks. *Coord. Chem. Rev.* 2017, 335, 28–43.
- (5) (a) Papanikolaou, D.; Kosaka, W.; Margadonna, S.; Kagi, H.; Ohkoshi, S.; Prassides, K. Piezomagnetic behavior of the spin crossover Prussian blue analogue CsFe[Cr(CN)₆]. *J. Phys. Chem. C* 2007, 111, 8086–8091. (b) Ohkoshi, S.; Imoto, K.; Tsunobuchi, Y.; Takano, S.; Tokoro, H. Light-induced spin-crossover magnet. *Nat. Chem.* 2011, 3, 564–569.
- (6) Muñoz-Lara, F. J.; Arcís-Castillo, Z.; Muñoz, M. C.; Rodríguez-Velamazán, J. A.; Gaspar, A. B.; Real, J. A. Heterobimetallic MOFs containing tetrathiocyanometallate building blocks: pressure-induced spin crossover in the porous {Fe^{II}(pz)[Pd^{II}(SCN)₄]} 3D Coordination Polymer. *Inorg. Chem.* 2012, 51, 11126–11132.
- (7) (a) Trzop, E.; Zhang, D.; Piñeiro-López, L.; Valverde-Muñoz, F. J.; Muñoz, M. C.; Palatinus, L.; Guerin, L.; Cailleau, H.; Real, J. A.; Collet, E. First step towards a devil's staircase in spin-crossover materials. *Angew. Chem., Int. Ed.* 2016, 55, 8675–8679. (b) Zhang, D.; Trzop, E.; Valverde-Muñoz, F. J.; Piñeiro-López, L.; Muñoz, M. C.; Collet, E.; Real, J. A. Competing phases involving spin-state and ligand structural orderings in a multistable two-dimensional spin crossover coordination polymer. *Cryst. Growth Des.* 2017, 17, 2736–2745.
- (8) Ortega-Villar, N.; Muñoz, M. C.; Real, J. A. Symmetry breaking in iron(II) spin-crossover molecular crystals. *Magnetochemistry* 2016, 2, 16.
- (9) Gülich, P.; Gaspar, A. B.; Ksenofontov, V.; García, Y. Pressure effects studies in molecular magnets. *J. Phys.: Condens. Matter* 2004, 16, S1087–S1108.
- (10) Gaspar, A. B.; Agustí, G.; Martínez, V.; Muñoz, M. C.; Levchenko, G.; Real, J. A. Spin Crossover Behaviour in the Iron(II)-2,2-dipyridilamine System: Synthesis, X-Ray Structure and Magnetic Studies. *Inorg. Chim. Acta* 2005, 358, 4089–4094.
- (11) Sciortino, N. F.; Neville, S. M.; Desplanches, C.; Léard, J. F.; Martínez, V.; Real, J. A.; Moubaraki, B.; Murray, K. S.; C. J. Kepert, C. J. An Investigation of Photo- and Pressure-Induced Effects in a Pair of Isostructural Two-Dimensional Spin-Crossover Framework Materials. *Chem. - Eur. J.* 2014, 20, 7448–7457.
- (12) (a) Decurtins, S.; Gülich, P.; Köhler, P. C.; Spiering, H.; Hauser, A. Light-induced Excited Spin State Trapping in a Transition-Metal Complex - the hexa-1-propyltetrazole-iron(II) tetrafluoroborate Spin-Crossover System. *Chem. Phys. Lett.* 1984, 105, 1–4. (b) Hauser, A. Reversibility of Light-induced Excited Spin State Trapping in the Fe(PTZ)₆(BF₄)₂ and the Zn_{1-x}Fe_x(PTZ)₆(BF₄)₂ Spin-Crossover Systems. *Chem. Phys. Lett.* 1986, 124, 543–548. Hauser, A. Light-Induced Spin Crossover and the High-Spin→Low-Spin Relaxation. *Top. Curr. Chem.* 2004, 234, 155–198.
- (13) Léard, J. F. Photomagnetism of Iron(II) Spin Crossover Complexes - the T(LIESST) Approach. *J. Mater. Chem.* 2006, 16, 2550–2559.
- (14) Sorai, M.; Nakano, M.; Miyazaki, Y. Calorimetric investigation of phase transitions occurring in molecule-based magnets. *Chem. Rev.* 2006, 106, 976–1031.
- (15) Léard, J. F.; Chastanet, G.; Guionneau, P.; Desplanches, C. Optimizing the stability of trapped metastable spin states. In *Spin-Crossover Materials, Properties and Applications*; Halcrow, M. A., Ed.; Wiley: Hoboken, NJ, 2013; pp 475–506.
- (16) Adams, C. J.; Muñoz, M. C.; Waddington, R. E.; Real, J. A. Cooperative spin transition in the two-dimensional coordination polymer [Fe(4,4'-bipyridine)₂(NCX)₂]_n·4CHCl₃ (X = S, Se). *Inorg. Chem.* 2011, 50, 10633–10642.
- (17) (a) Real, J. A.; Andrés E.; Muñoz, M. C.; Julve, M.; Granier, T.; Bousseksou, A.; Varret, F. Spin crossover in a catenane supramolecular system. *Science* 1995, 268, 265–267. (b) Romero-Morcillo, T.; De la Pinta, N.; Callejo, M. L.; Piñeiro-López, L.; Muñoz, M. C.; Madariaga, G.; Ferrer, S.; Breczewski, T.; Cortes R.; Real, J. A. Nanoporosity, inclusion chemistry, and spin crossover in orthogonally interlocked two-dimensional metal-organic frameworks. *Chem. - Eur. J.* 2015, 21, 12112–12120.
- (18) Yang, F.-L.; Chen, M.-G.; Li, X.-L.; Tao, J.; Huang, R.-B.; Zheng, L.-S. Two-dimensional iron(II) networks-guest-dependent structures and spin-crossover behaviors. *Eur. J. Inorg. Chem.* 2013, 2013, 4234–4242.
- (19) Miyaura, N.; Suzuki, A. Palladium-catalyzed cross-coupling reactions of organoboron compounds. *Chem. Rev.* 1995, 95, 2457–2483.
- (20) Sheldrick, G. M. *SHELXL-2014*; University of Göttingen, Göttingen, Germany, 2014.